LASER & PHOTONICS REVIEWS

www.lpr-journal.org

Stereo Jones Matrix Holography with Longitudinal Polarization Transformation

Ruizhe Zhao, Qunshuo Wei, Yuzhao Li, Xin Li, Guangzhou Geng, Xiaowei Li, Junjie Li, Yongtian Wang, and Lingling Huang**

Metasurfaces have exhibited powerful abilities for manipulating multiple fundamental properties of light including amplitude, phase, polarization, and so on. However, these strategies are commonly concentrated on the modulations at a single transverse plane of output light. The spatial evolutions of these properties, especially the polarizations along longitudinal direction, are rarely investigated. Here, a stereo Jones matrix holography method is presented for understanding the spatial evolution including polarization, amplitude, and phase variations along the longitudinal direction. Stereo holographic algorithms in matrix framework are developed to generate multiplane and even continuously varied vectorial holographic images that exhibit distinct polarization states at each transverse plane. This method provides a benchmark of longitudinal polarization transformations as well as beam modulations by simply using a single planar metasurface without extra burdens on optical path. In addition, the obtained propagation-dependent features can favor the realizing of on-demand transverse and longitudinal spatial evolution from the perspective of the holographic method. Furthermore, it may also promote the development of related areas including polarization-switchable devices, optical trapping, microscopy, laser processing, etc.

1. Introduction

Versatile manipulation of amplitude, phase, polarization within stereo 3D space and their characterization are crucial ultimate goals for spatial beam shaping. The propagation-dependent polarization characteristic provides another degree of freedom (DOF) for realizing high-dimensional structured light (integrating with other DOFs including phase, space, temporal, and so on) and offer new opportunities for light–matter interactions.[1,2] However, beams that propagating in free-space without disturbance usually preserve their polarization states during propagation. The common strategy for polarization manipulation is to spatially tailor the orthogonal polarization basis components with different amplitude ratio and phase delay while conserving its global energy. Traditionally, the polarization rotation phenomenon can be induced by inserting birefringent materials with optical activity.[3] While, this manner is inconvenient and the optical activity of natural materials are limited. In order to solve this limitation, some methods have been demonstrated for generating vector beams with variant polarization states upon propagations such as by utilizing radial-to-longitudinal mapping of axicon phase,[4] superposing amplitude modulated beams,[5,6] and introducing varying phase difference along propagation direction.[7,8] Nevertheless, these proposed schemes are still cumbersome and bulky optical setups are required.

The innovative platform of metasurfaces can flexibly manipulate the fundamental properties of light, including amplitude,[9,10] phase,[11,12] polarization,[13,14] orbital angular momentum,[15,16] and even simultaneous multiple parameters with subwavelength resolution.[17–19] Such manipulations of wavefront prompt the developments of substantial applications in the areas of beam shaping,[20,21] metalens,[22,23] holography,[24–26] nonlinear optics,[27,28] polarization generation and detection,[29,30] etc. Recent advances have enabled spatially variant polarization distribution of light within a single transverse plane. Cylindrical vector beams,[13,31] vector vortex beams,[32,33] as well as Poincaré beams[34,35] are generated by using locally varying anisotropic meta-atoms within 2D

R. Zhao, Q. Wei, Y. Li, X. Li, Y. Wang, L. Huang
Beijing Engineering Research Center of Mixed Reality and Advanced Display
Key Laboratory of Photoelectronic Imaging Technology and System of Ministry of Education of China
School of Optics and Photonics
Beijing Institute of Technology
Beijing 100081, China
E-mail: wyt@bit.edu.cn; huanglingling@bit.edu.cn

G. Geng, J. Li
Beijing National Laboratory for Condensed Matter Physics
Institute of Physics, Chinese Academy of Sciences
Beijing 100191, China

X. Li
Laser Micro/Nano-Fabrication Laboratory
School of Mechanical Engineering
Beijing Institute of Technology
Beijing 100081, China

The ORCID identification number(s) for the author(s) of this article can be found under https://doi.org/10.1002/lpor.202200982

DOI: 10.1002/lpor.202200982

arrays. Meanwhile, holographic images with tailored polarization distribution dubbed vectorial holography are successfully demonstrated based on segmented,[36,37] interleaved[38,39] or noninterleaved metasurfaces.[40–43] For the nonmultiplexing schemes, the deliberately designed polarization distributions are commonly accomplished by linking the desired polarization states with the Jones matrix at metasurface plane or utilizing two transmitted/deflected beams from sub-units of the metasurface.[40–44] However, most of the existing strategies are devoted to achieve vectorial holography at individual image plane. Based on a form-birefringent metasurface, arbitrary polarization responses can be imposed to a propagation Bessel beam which dramatically decrease the complexity of the required optical system in traditional strategies.[45] Nevertheless, previous reports lack the abilities to generate 3D holographic images with stereo independently controlled polarizations.[46–48] Such polarization transformation in longitudinal propagation-direction brings big challenge of static metasurfaces.

Here, we present a stereo Jones matrix method for understanding the spatial evolution including polarization, amplitude, and phase transformations along the longitudinal direction by integrating traditional holographic algorithm with Jones matrix method. Remarkably, such stereo Jones matrix holography can impart arbitrarily chosen polarization responses along longitudinal direction within a single layer form-birefringent metasurface. Multiplane holographic images that exhibit distinct polarization states at each transverse plane are successfully obtained with the assistance of the imposed polarization responses. In the experiment, the Lu-Chipman decomposition method is utilized to extract the retardance and fast-axis orientation of the measured Mueller matrix at each pixel of different image planes for proving the effectiveness of our demonstrated method. Furthermore, a three-turn hollow helix pattern with longitudinally continuous polarization transformations is successfully reconstructed based on a vectorial point source method. The realization of such stereo vectorial holographic image successfully represents the 3D propagation evolution of multiple properties of light and expands the limitations of traditional scalar diffraction law. Such technique allows the metadevice to respond with different yet completely determined wavefront along the optical path, which may bring completely novel functionalities in light–matter interaction, optical manipulation as well as quantum optics.

2. Principle

Our objective is to realize stereo vectorial holographic images with longitudinally variable polarization distributions without extra burdens on the optical path. The amplitude, phase, and polarization of wavefront located at different z-position can be tailored at will. For achieving such intriguing functionality, the vital process is to integrate the traditional stereo holographic algorithms with Jones matrix method. We concentrate on imposing distinct polarization responses on each image plane together with the amplitude and phase modulations. Therefore, multiple fundamental properties of light can be simultaneously controlled with custom-defined properties within 3D space.

The generalized design principle of our demonstrated stereo Jones matrix holography method is illustrated in **Figure 1**. A 3D holographic image with spatially continuous polarization states along longitudinal direction can be successfully obtained. This is because the desired phase and amplitude distributions as well as polarization responses are imposed at individual transverse plane, forming a 3D matrix framework of wavefront with rigorous mathematical and physical restrictions along the longitudinal direction. By considering these restrictions in the stereo transmission space, the vectorial Jones matrix in the metasurface plane can be calculated using backward propagation as follows

$$\tilde{\mathbf{J}}_{meta}(x,y) = \mathcal{H}\left\{\begin{matrix} A_1(x,y)e^{i\varphi_1(x,y)}\tilde{\mathbf{P}}_1(x,y), A_2(x,y)e^{i\varphi_2(x,y)}\tilde{\mathbf{P}}_2(x,y), \\ \cdots, A_N(x,y)e^{i\varphi_N(x,y)}\tilde{\mathbf{P}}_N(x,y) \end{matrix}\right\} = \tilde{\mathbf{H}}_{meta}\tilde{\mathbf{U}}_{meta} \quad (1)$$

where $\mathcal{H}$ represents propagation kernel function, A_n and φ_n represent the amplitude and phase distributions within the nth ($n = 1,2,3, \ldots, N$) transverse plane, $\tilde{\mathbf{P}}_n$ is the imposed polarization responses (function as a polarizer, wave-plate or any other polarization elements that represented by symmetric Jones matrices) to each transverse plane. Such spatially variant restrictions of each transverse plane along longitudinal direction forms the 3D framework. For arbitrary Jones matrix $\tilde{\mathbf{J}}_{meta}$, it can be represented by the production of a Hermitian matrix $\tilde{\mathbf{H}}_{meta}$ (diattenuator) and a unitary matrix $\tilde{\mathbf{U}}_{meta}$ (retarder) based on matrix polar decomposition. Hence, by setting smoothly and continuously changed wavefront (solution of Maxwell equation) in stereo space, one can always be able to generate vectorial Jones matrix on a single layer metasurface. While for some counter-intuitive or suddenly changed spatial structured light, extra effort should be made by using optimization or holographic based methods for achieving such spatial evolution on-demand.

Note one can impose arbitrary amplitude, phase, and polarization restriction (represented by a symmetric Jones matrix) to form the stereo Jones matrix holography. And vectorial Fresnel diffraction formula, angular spectrum method, or point source algorithm can be used for the propagation process (by designing the propagation kernel function H). While the desired arbitrary polarization response $\tilde{\mathbf{P}}_n$ (symmetric property $P_{12\_n} = P_{21\_n}$) has different forms and functions as essential restrictions to distinguish from other scalar wavefront evolution

$$\tilde{\mathbf{P}}_n = \begin{bmatrix} P_{11\_n} & P_{12\_n} \\ P_{21\_n} & P_{22\_n} \end{bmatrix} = \tilde{\mathbf{H}}_n\tilde{\mathbf{U}}_n \quad \left(e.g.\ \tilde{\mathbf{P}}_n = \begin{bmatrix} i\cos(2\theta_{f,n}) & i\sin(2\theta_{f,n}) \\ i\sin(2\theta_{f,n}) & -i\cos(2\theta_{f,n}) \end{bmatrix}\right) \quad (2)$$

Here, we choose the polarization response of a half-wave plate (HWP) as an example and the $\theta_{f,n}$ in Equation (2) refers the fast-axis orientation of a half-wave plate. Similarly, $\tilde{\mathbf{P}}_n$can be decomposed to a Hermitian matrix $\tilde{\mathbf{H}}_n$ and a unitary matrix $\tilde{\mathbf{U}}_n$,representing the polarization-dependent amplitude and phase modulations in matrix framework. Other types of polarization responses including polarizer, quarter-wave plate or the polarization transforms are still effective in our proposed scheme (detail information is provided in the Supporting Information).

To form the Jones matrix holography, usually iterative loops between the hologram plane and different planes should be set.

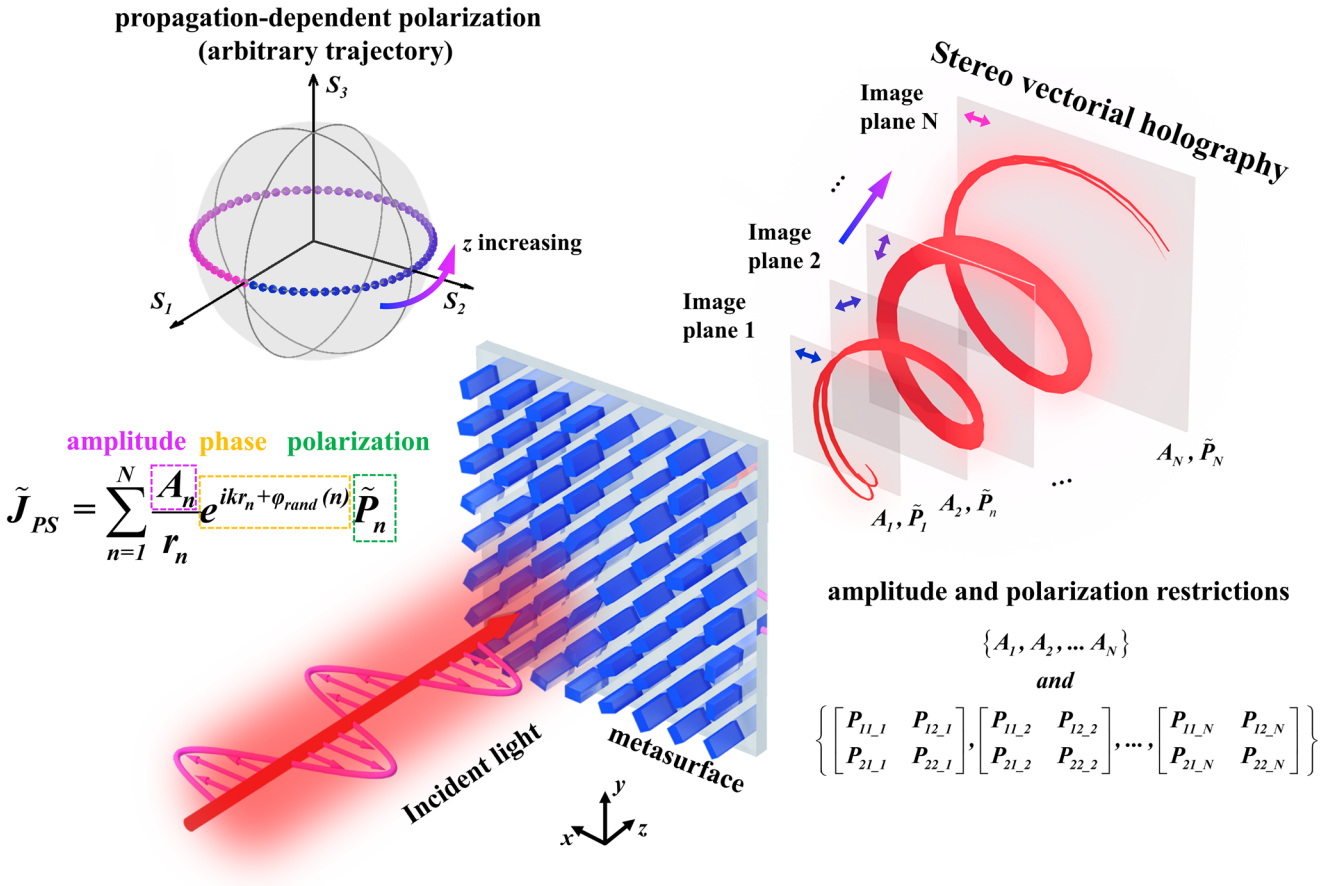

Figure 1. Schematic illustration of stereo vectorial holographic images with longitudinal polarization transformation. Arbitrary phase, amplitude, and polarization restrictions in each transverse planes are imposed, forming a 3D matrix framework of wavefront with rigorous mathematical and physical restrictions along the propagation direction. A three-turn hollow helix pattern with continuous varied polarization states (covering entire equator of the Poincaré sphere) along optical path can be obtained.

After sufficient iterations, the unitary part $\tilde{\mathbf{U}}_{meta}$ of calculated matrix distribution $\tilde{\mathbf{J}}_{meta}$ at hologram plane can be encoded to a form-birefringent metasurface by discarding the Hermitian part. Because the realization of the complete calculated matrix $\tilde{\mathbf{J}}_{meta}$ is difficult which may need hybrid metasurface composed of both plasmonic/lossy (Hermitian response) and dielectric (unitary response) meta-atoms or cascaded metasurface (one layer for Hermitian response, the other layer for unitary response). While such discarding processes is similar to acquiring the phase-only hologram from the calculated complex amplitude distribution and in favor of acquiring the desired polarization responses within a single layer metasurface by preserving the high quality with longitudinally vectorial feature.

We first set a multiple-plane vectorial holography as an example. The holographic images with distinct polarization states at different image planes are obtained by developing a multiplane holographic algorithm in matrix framework. The flowchart of the algorithm is shown in **Figure 2**. For the initialization, the 2×2 unitary matrix at each pixel is randomly generated. We use $\tilde{\mathbf{U}}_{meta}$ to represent the matrix array that composed of 1000×1000 unitary matrices. In each iteration, the propagation from hologram plane to different image planes is calculated by the Fresnel diffraction formula in the form of Fourier transform (FrT)

$$\tilde{\mathbf{B}}_n(x_o, y_o) = \frac{\exp(jkz)}{j\lambda z} \exp\left[\frac{jk}{2z}(x_o^2 + y_o^2)\right] \times F\left\{\tilde{\mathbf{U}}_{meta}(x_h, y_h) \exp\left[\frac{jk}{2z}(x_h^2 + y_h^2)\right]\right\} \quad (3)$$

where $\tilde{\mathbf{B}}_n$ ($n = 1, 2, \ldots, N$ represents different planes) is the Jones matrix at the nth plane, k is the wave vector, z refers the propagation distance, (x_h, y_h) and (x_o, y_o) represent the coordinates of the hologram plane and the image plane. The Jones matrix at each pixel of these three individual object planes are calculated parallelly and denoted by $\tilde{\mathbf{B}}_1$ to $\tilde{\mathbf{B}}_N$. Note the plane number is not limited indeed. Meanwhile, matrix polar decomposition method is adopted to acquire the corresponding Hermitian part $\tilde{\mathbf{H}}_n$ and unitary part $\tilde{\mathbf{U}}_n$ of each transverse plane. The desired amplitude distribution A_n of original image and polarization response $\tilde{\mathbf{P}}_n$ are imposed as the restrictions at each image plane based on Equation (1). And the backward propagation process is realized based

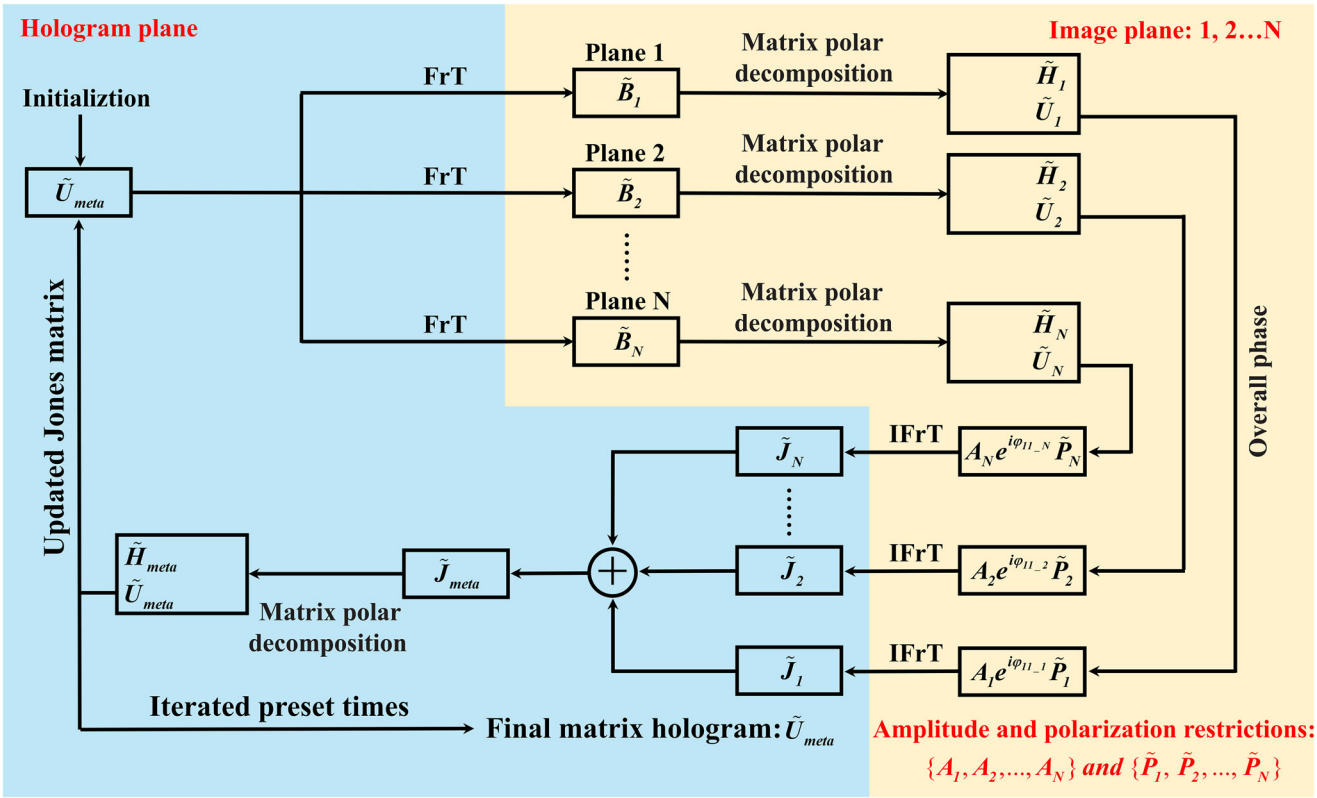

Figure 2. The flowchart of a Jones matrix holographic algorithm framework for obtaining multiplane holographic images with propagation-dependent polarization transformations. The number of total image planes is represented by *N*. The FrT and IFrT represent the Fresnel transform and inverse Fresnel transform in matrix framework, respectively.

on the Inverse Fresnel transform (IFrT) method. After backward propagation, the corresponding Jones matrices $\tilde{\mathbf{J}}_{meta}$ at the hologram plane are obtained by combining the calculated matrices $\tilde{\mathbf{J}}_1$, $\tilde{\mathbf{J}}_2$ ... $\tilde{\mathbf{J}}_N$ from each image plane which can be expressed as follow

$$\tilde{\mathbf{J}}_{meta}(x_h, y_h) = \sum_{n=1}^{N} -\frac{\exp(-jkz_n)}{j\lambda z_n} \exp\left[-\frac{jk}{2z_n}(x_h^2 + y_h^2)\right] \times F^{-1}\left\{\tilde{\mathbf{C}}_{\mathbf{n}}(x_o, y_o)\right\} \tag{4}$$

$$where\ \tilde{\mathbf{C}}_{\mathbf{n}}(x_o, y_o) = A_{\mathrm{n}}(x_o, y_o) e^{i\varphi_{11\_n}(x_o, y_o)} \tilde{\mathbf{P}}_{\mathbf{n}}(x_o, y_o) \exp\left[-\frac{jk}{2z_{\mathrm{n}}}(x_{\mathrm{o}}^2 + y_{\mathrm{o}}^2)\right]$$

where A_n refers the amplitude distribution of desired image at plane *n*. The phase item $\varphi_{11\_n}(x_0, y_0)$ of upper left element of $\tilde{B}_{\mathbf{n}}(x_o, y_o)$ is extracted as the overall phase. At the hologram plane, we extract the unitary part of $\tilde{\mathbf{J}}_{meta}$ as the updated unitary Jones matrix for the next iteration. And the desired unitary matrix hologram $\tilde{\mathbf{U}}_{meta}$ is successfully obtained by discarding the Hermitian part of $\tilde{\mathbf{J}}_{meta}$ after a sufficient number of iterations (50 times). The entire process takes nearly 1400 s in a personal computer (Central Processing Unit (CPU): Intel i7 11700KF). Noted that, the global efficiencies at different planes can be arbitrarily predesigned by multiplying a series of coefficients to the amplitude restrictions and can be expressed by $\{c_1A_1, c_2A_2, \cdots, c_nA_N\}$. The suitable chosen coefficients in favor of compensating the energy loss during propagating and balancing the energy distributions between different image planes.

Alternatively, by developing a vectorial point source algorithm, for each individual point source on the image plane, the radiation to the hologram plane can be expressed as follows

$$\tilde{\mathbf{J}}_{PS} = \sum_{\mathrm{n}=1}^{N} \frac{\mathrm{A}_n}{r_n} \mathrm{e}^{ikr_n + \varphi_{rand}(n)} \tilde{\mathbf{P}}_n \tag{5}$$

where *N* is the number of the composed point sources, A_n is the amplitude of the point source, r_n ($\mathrm{r_n} = \sqrt{(x_\mathrm{h} - x_\mathrm{n})^2 + (\mathrm{y}_h - y_n)^2 + (\mathrm{z}_h - z_n)^2}$) refers the distance between the point sources within 3D space and the hologram plane. Especially, a random phase distribution $\varphi_{\mathrm{rand}}(n)$ for each point source is added for obtaining a more uniform amplitude distribution. We design a three-turn hollow helix with continuously varied polarization states along longitudinal direction by imposing the essential amplitude, phase and polarization response restrictions to each point source.

After generating the vectorial Jones matrix distribution, the calculated unitary matrix $\tilde{\mathbf{U}}_{meta}$ at each pixel of the hologram plane can be implemented based on form-birefringent metasurface

$$\tilde{\mathbf{U}}_{meta} = R(\theta) \begin{bmatrix} e^{i\varphi_x} & 0 \\ 0 & e^{i\varphi_y} \end{bmatrix} R(-\theta) \tag{6}$$

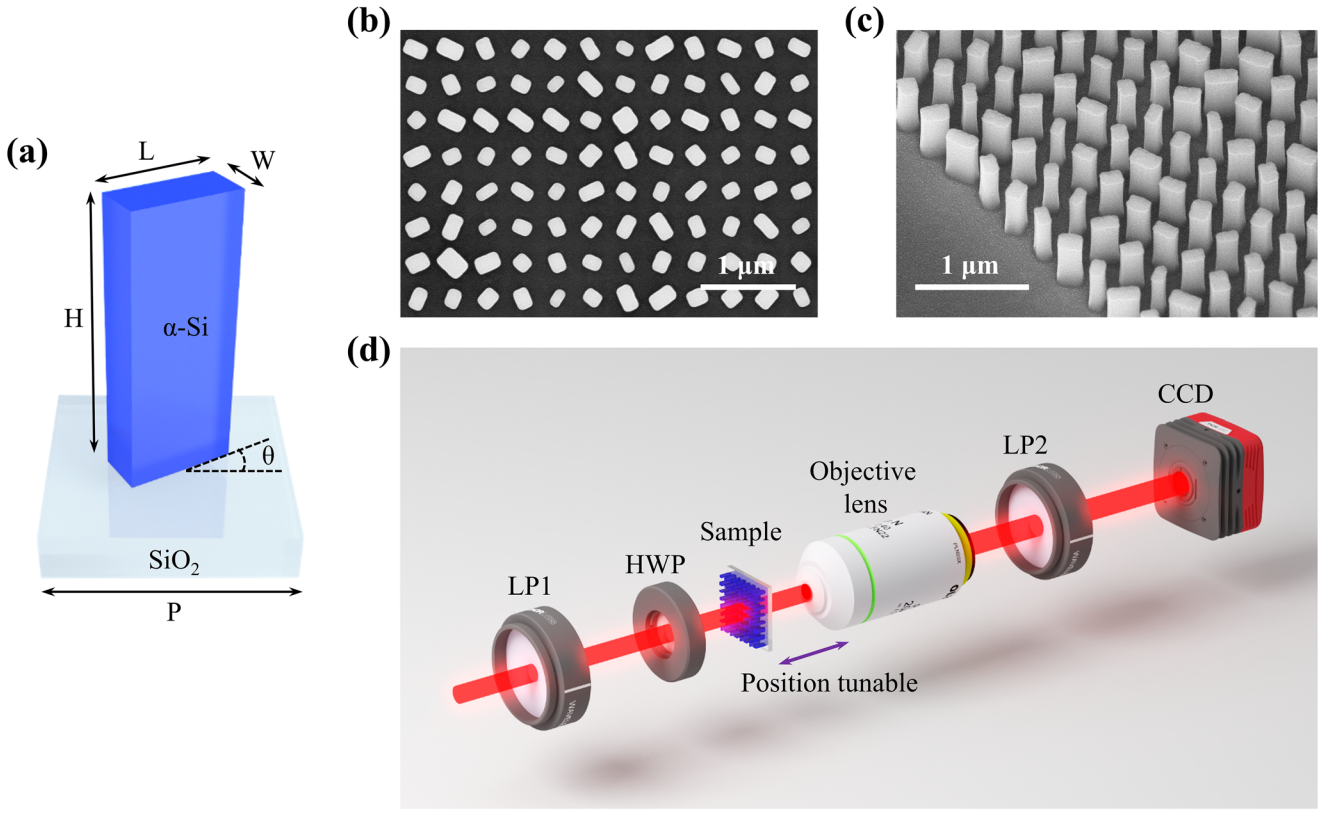

Figure 3. Fabricated samples and experiment setup. a) Schematic of meta-atom. We use α-Si nanofin arrays located on a fused quartz substrate to compose the metasurface. b,c) The scanning electron microscopy images of our fabricated metasurface sample 1 in top and side view. d) The experimental setup. An objective lens (20 × /NA = 0.45) and a charge coupled device camera (CCD) constitute the imaging system. Images located at different planes are captured by adjusting the distances between the metasurface and the imaging system based on a manual stage that manufactured by DAHENG OPTICS (GCM-TP13ML).

The polarization-dependent phase shift (φ_x, φ_y) is acquired by calculating the eigenvalues of $\tilde{U}_{\text{meta}}$. Meanwhile, the $R(\theta)$ which indicates a rotation matrix can be acquired by the corresponding eigenvectors. Hence, one can use simple nanofins with rectangular cross-section for implementing such vectorial Jones matrix accordingly.

3. Experiment

For the purpose of experimental demonstration, two metasurfaces named sample 1 and sample 2 are fabricated on a fused quartz substrate based on electron beam lithography as well as inductively coupled plasma reactive ion etching method (detail information is provided in Supporting Information). The schematic structure is depicted in **Figure 3**a. The scanning electron microscopy images of sample 1 with a top view and side view are shown in Figure 3b,c. The experimental setup that utilized to capture the reconstructed holographic images are illustrated in Figure 3d (detail information is provided in the Experimental Section).

In the process of designing sample 1, three capitalized alphabets "B," "I," and "T" are chosen as the original images and are located at different positions along z-direction (z_B = 300 μm, z_I = 400 μm, and z_T = 500 μm). The polarization responses of different holographic images can be manipulated simultaneously by integrating traditional holographic algorithm with Jones matrix method as demonstrated above. Especially, the three holographic images can function as half-wave plates with different fast-axis orientations ($\theta_{f\text{-}B}$ = 0°, $\theta_{f\text{-}I}$ = 30°, and $\theta_{f\text{-}T}$ = 45°) at different z planes in our design. Hence, the exhibited polarization states under incident light with different polarizations $|E_{in}\rangle$ can be calculated accordingly. Meanwhile, we balance the global efficiencies of different image planes by choosing suitable coefficients $\{c_1$=0.3, c_2= 0.55, c_3=1$\}$. Noted that the number of vectorial planes N is not limited to three (some discussions about the factors that affect the number of image plane are provided in Section E of the Supporting information). The simulated and experimental results of sample 1 for achieving multiplane vectorial holographic images under x-linearly polarized light illuminating are depicted in **Figure 4**. By adjusting the distance between the metasurface sample and the imaging system based on a manual translation stage (DAHENG OPTICS, GCM-TP13ML), three holographic images ("B," "I," and "T") that located at 289, 377, and 481 μm are successfully captured with good qualities and agree well with the simulated results as depicted in Figure 4a–f. The slight deviation of the locations between the experiment and theoretical design may originate from the precision of the manual translation stages as well as the process of estimating the location from the scale of the manual translation stages. Meanwhile,

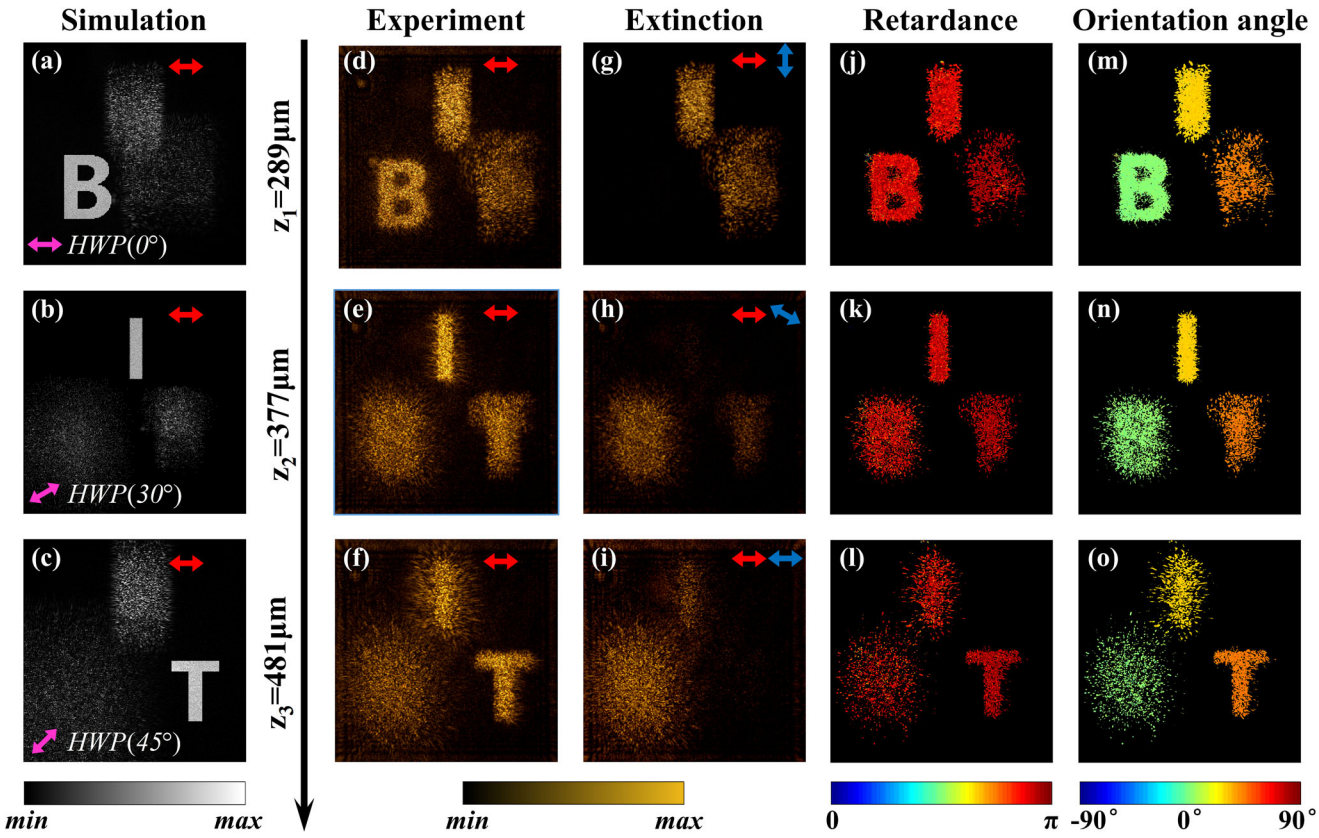

Figure 4. Experimental results of multiplane vectorial holography. a–f) Simulated and experimental results of the multiplane holographic images with propagation-dependent polarization. Each holographic image can function as a half-wave plate with different fast-axis orientation (indicated by the pink arrows). g–i) The extinct phenomena when rotating the transmission axis of LP2 to the orthogonal direction (to 90°, 120°, and 135° successively), which clearly demonstrate that the holographic images can exhibit distinct polarization states at each transverse plane along longitudinal direction. j–l) The derived retardance distribution from measured Mueller matrix at each pixel of different planes. m–o) The derived fast-axis orientation angle distribution from measured Mueller matrix. The red and blue arrows indicate the polarization of input and output light.

we demonstrate that each holographic image can act as a half-wave plate with specific fast-axis orientation angle. The imposed polarization responses make the holographic images exhibit linear polarization states with various orientation angle ($\theta_{p\text{-}B} = 0°$, $\theta_{p\text{-}I} = 60°$, and $\theta_{p\text{-}T} = 90°$). In the experiment, a polarization analyzer is used to distinguish the polarization state at different image planes. As shown in Figure 4g–i, the captured holographic images can be extinguished when the polarizer is rotated to specific orientation at each image plane. The expected extinct phenomena agree well with the theoretical predictions.

In order to further prove such propagation-dependent vectorial feature, we acquire the Mueller matrix at each pixel of individual image plane by measuring the intensity distributions under different input/output polarization combinations[43] (detailed information is provided in the Supporting Information). Then, each Mueller matrix is analyzed by using the Lu-Chipman Decomposition method. This method is commonly adopted for extracting different polarization properties including diattenuation, retardance and depolarization from given Mueller matrices.[49] We obtain the retarder matrix $\tilde{\mathbf{M}}_{R,n}$ at each pixel of image plane n according to the measured intensity distributions that shown in Figures S2–S4 in the Supporting Information based on the decomposition method. The derived retardance R_n (phase difference between fast- and slow-axis of a waveplate) and fast-axis orientation angle $\theta_{f,n}$ of $\tilde{\mathbf{M}}_{R,n}$ can be expressed as follow

$$R_{\mathrm{n}} = \cos^{-1}\left[\frac{tr(\tilde{\mathbf{M}}_{R,n})}{2} - 1\right] \tag{7}$$

$$\theta_{f,n} = \frac{1}{2\sin R_{\mathrm{n}}}\sum_{j,k=1}^{3}\epsilon_{ijk}(\tilde{\mathbf{m}}_{R,n})_{jk} \tag{8}$$

where ϵ_{ijk} is the Levi-Civita permutation symbol and $\tilde{\mathbf{m}}_{R,n}$ refers a 3×3 matrix that obtained by striking out the first row and column of $\tilde{\mathbf{M}}_{R,n}$. At each image plane, the derived retardance R_n and fast-axis orientation distributions $\theta_{f,n}$ are shown in Figure 4j–o. The values of retardances are close to π and the derived fast-axis orientations of each holographic image are as expected. These measured results are consistent well with the corresponding theoretical results in acceptable deviation tolerance. Meanwhile, in the experiment, the measured transmission efficiency of sample 1 is 32.02%. And the broadband property when changing the wavelength of incident light from 740 to 840 nm is provided in Section F of Supporting Information. The broadband property arises from the robustness of our silicon metasurface holograms as well

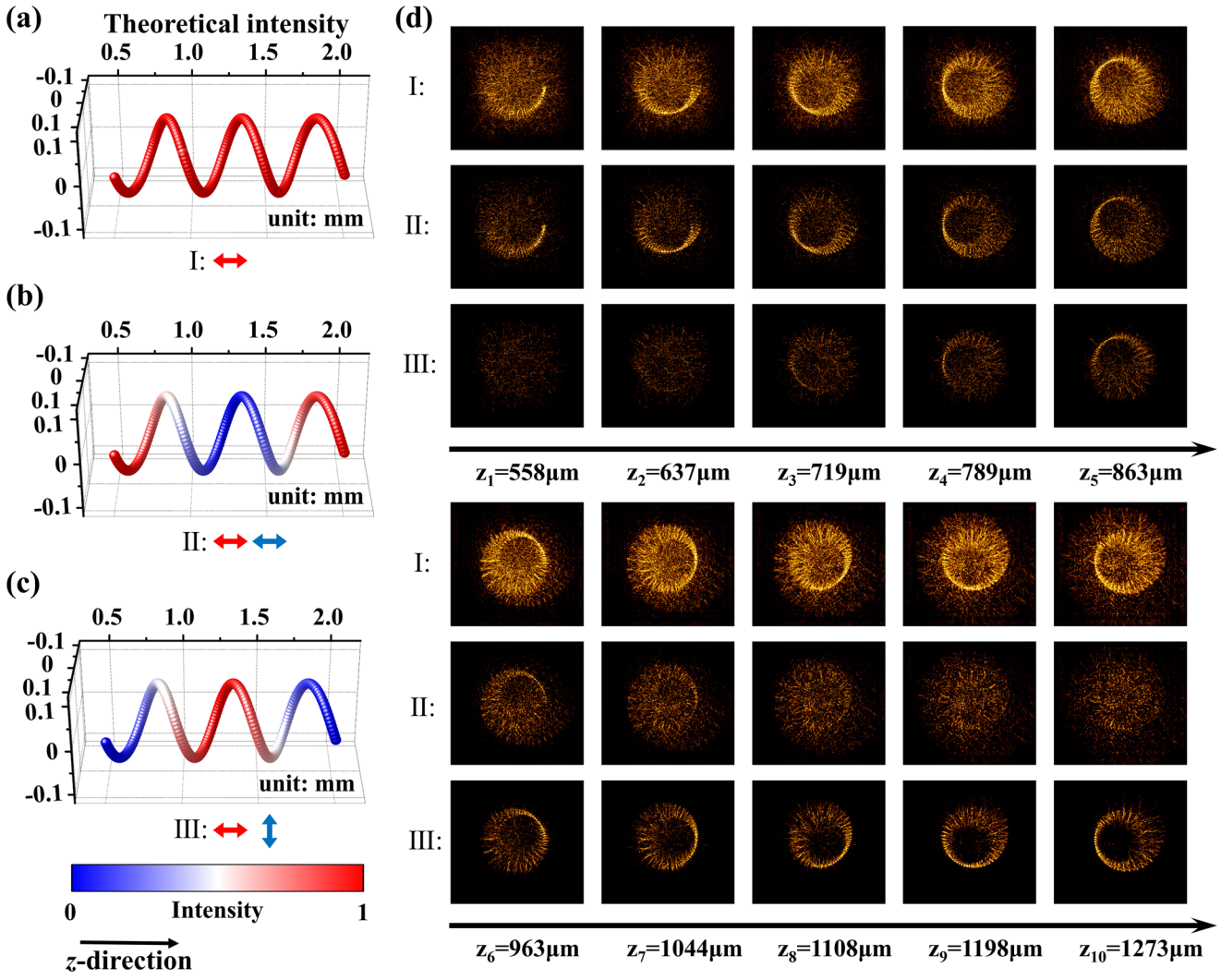

Figure 5. Experimental results of stereo Jones matrix holography with longitudinally varying polarization transformations. a–c) Theoretical intensity distributions of the helix pattern along *z*-direction under different configurations of LP1 (I, II, III: with LP1, transmission axis: 0°) and LP2 (I: without LP2, II: with LP2, transmission axis: 0°, III: with LP2, transmission axis: 90°) based on Malus's law. The red and blue arrows indicate the polarization of input and output light. d) The polarization detection results of the three-turn hollow helix pattern with spatially continuous polarization states along longitudinal direction under different configurations of LP1 and LP2. Such measured intensity distributions successfully demonstrate the evolution of polarization along longitudinal direction.

as the acceptable phase difference distribution of the α-Si nanofin with different dimensions when changing the wavelength of incident light.[40]

Furthermore, another fabricated metasurface sample 2 is utilized to demonstrate that our design strategy is capable of generating stereo holographic images with continuously varied polarization transformations. A three-turn hollow helix pattern with its helix axis along *z*-direction is selected as the reconstructed 3D image as shown in **Figure 5**a. The pitch and diameter of this pattern are 500 and 150 μm, respectively. The helix pattern is composed of 200 point sources (located in the range of 500 to 2000 μm) which can function as a series of half-wave plates with continuous varied fast-axis orientation angles (from 0° to 90°) in equal interval. Hence, the corresponding polarization states of these point sources are all linear polarization states varying gradually from 0° to 180° (covering entire equator of the Poincaré sphere) under *x*-linearly polarized light illuminating. The theoretical intensity distributions of the helix pattern along *z*-direction under different input/output polarization configurations are illustrated in Figure 5a–c based on Malus's law ($I = I_0\cos^2(\theta_p)$, θ_p is the angle between the polarization orientation and transmission axis of polarization analyzer).

In the experiment, we capture ten individual image planes within different *z* positions (from 558 to 1273 μm) by adjusting the distance between the metasurface and the imaging system. The obtained reconstructed images are shown in Figure 5d. We can find that different components of the helix become clear at different *z* positions. In the first 1.5 turn, the theoretical polarization state of each point source is continuously varying from *x*-linear polarization to *y*-linear polarization state. Similarly, one can analyze the inhomogeneous polarization distribution along propagation-direction. Under the analyzer LP2 with horizontal

transmission axis (case II), the intensities of the point sources at each image plane are gradually attenuating by increasing the distance in z-direction due to the Malus's law. Meanwhile, the changes of the intensities are reversed when rotating the transmission axis to orthogonal direction (case III). These phenomena are observed based on the spatially varied vectorial characteristic of different point sources along propagation-direction. Such experimental results are consistent with the theoretical results and can prove that stereo vectorial holography is successfully demonstrated based on the vectorial point source algorithm in matrix framework. In addition, the evolution processes of the total three-turn helix pattern with and without the polarization analyzer when adjusting the distance in z-direction are provided in the videos of the Supporting Information.

4. Discussion

In summary, we have demonstrated a novel method for achieving stereo Jones matrix holography with propagation-dependent polarization states based on dielectric metasurfaces. Multiplane vectorial holographic images and even 3D helix with continuously varied polarization states along longitudinal direction are successfully obtained. This method is very distinct from majority of previous works that acquire vectorial holographic within a single plane or identical polarization states of multiplanes along z-direction.[46–48] Meanwhile, holographic images with arbitrary polarization transformations including circular polarization and elliptical polarization states are also achievable in our scheme (more details are provided in section C of Supporting Information). In addition, the inhomogeneous polarization distribution of the reconstructed image at individual image plane can also be realized as demonstrated in Section D of Supporting Information. That is, such method can generate holographic images with both transversely and longitudinally variable polarization distributions. Recently, some methods have demonstrated the realization of arbitrary unitary matrix based on bilayer structures.[50,51] While, our article focuses on generating arbitrary polarization states along propagation direction by utilizing the imposed polarization restriction $\tilde{\mathbf{P}}_{\mathrm{n}}$ (expressed by a unitary and symmetric Jones matrix) based on single layer metasurface with controllable linear birefringence.

Furthermore, such method may also offer a distinctive way to investigate the stereo spatial evolution including polarization, amplitude and phase variations along the propagation direction which in favor of realizing high-dimensional structured light in the perspective of holographic method. Such functionality is highly desired for generating complex optical field within compact optical systems. Especially, the propagation-dependent features may provide another degree of freedom for applications including polarization-switchable devices, optical trapping, microscopy, as well as laser processing.

5. Experimental Section

Implementation of Metasurface Design: α-Si nanofin arrays located on a fused quartz substrate were adopted to compose the metasurface. The high-index α-Si nanofin can be treated as a tiny waveguide and exhibit different effective refractive index (n_{eff}) along its long and short axis. Based on these form birefringence phenomena, arbitrary phase shifts can be imposed on the orthogonal polarization components of output light by tailoring the geometric dimension of nanofin.

A 2D parameter optimization is carried out by sweeping the length L and width W of the nanofin in the range of 60–280 nm with an interval of 5 nm based on rigorous coupled wave analysis method. The working wavelength is fixed at 800 nm due to the low loss of α-Si in near-infrared region. And the corresponding refractive index of amorphous silicon and substrate are set as $n_{\mathrm{Si}} = 3.802$ and $n_{\mathrm{sub}} = 1.5$ in the simulation. The calculated amplitude ($\mathrm{abs}(t_{xx})$ and $\mathrm{abs}(t_{yy})$) and phase (φ_x and φ_y) of the transmission coefficients t_{xx} and t_{yy} are shown in Figure S1 in the Supporting Information. In order to eliminate the undesired high diffraction orders as well as cover the phase shift from 0 to 2π, the period P and height H of the α-Si nanofin are chosen as 400 and 600 nm, respectively. At each pixel, the orientation angle of the α-Si nanofin is given by the corresponding rotation matrix $R(\theta)$. Meanwhile, the size of nanofin is determined from the simulated results by guaranteeing the minimum of the error $\varepsilon = abs(t_{xx} - \exp(i\phi_x)) + abs(t_{yy} - \exp(i\phi_y))$. The proposed metasurface is composed of 1000×1000 α-Si nanofins with different sizes (L, W: 60–280 nm, H: 600 nm, and P: 400 nm) and orientation angles (θ: −90°–90°).

Optical Measurement: The experimental setup used in the experiment is shown in Figure 3d. Light from a laser source passes through a linear polarizer LP1 and a HWP. The LP1 and HWP are used together to manipulate the polarization state of incident light. An objective lens ($20\times$/NA = 0.45), and a charge coupled device camera (CCD) constitute the image system. The reconstructed holographic images located at different image planes are captured by adjusting the distance between the metasurface and the imaging system based on a manual translation stage (DAHENG OPTICS, GCM-TP13ML). Another linear polarizer LP2 is used as an analyzer to discriminate the vectorial feature of the reconstructed images.

Supporting Information

Supporting Information is available from the Wiley Online Library or from the author.

Acknowledgements

The authors acknowledge the funding provided by the National Key R&D Program of China (2021YFA1401200), Beijing Outstanding Young Scientist Program (BJJWZYJH01201910007022), National Natural Science Foundation of China (Nos. U21A20140 and 92050117) program, Fok Ying-Tong Education Foundation of China (No. 161009), and Beijing Municipal Science and Technology Commission, Administrative Commission of Zhongguancun Science Park (No. Z211100004821009). This work was supported by the Synergetic Extreme Condition User Facility. The authors also acknowledge the fabrication and measurement service in the Analysis and Testing Center, Beijing Institute of Technology.

Author Contributions

L.H. and R.Z. proposed the idea; R.Z. conducted pattern designs and numerical simulations; R.Z., Q.W., and X.L. conducted the hologram generations; G.G. and J.L. fabricated the samples; R.Z. and Y.L. performed the measurements; and R.Z. and L.H. prepared the paper. L.H. and Y.W. supervised the overall projects. All the authors analyzed the data and discussed the results.

Conflict of Interest

The authors declare no conflict of interest.

Data Availability Statement

The data that support the findings of this study are available from the corresponding author upon reasonable request.

Keywords

metasurfaces, polarization transformation, stereo Jones matrix holography

Received: December 14, 2022
Published online:

[1] C. He, Y. Shen, A. Forbes, *Light: Sci. Appl.* **2022**, *11*, 205.
[2] A. Forbes, M. de Oliveira, M. R. Dennis, *Nat. Photonics* **2021**, *15*, 253.
[3] L. D. Barron, *Molecular Light Scattering and Optical Activity*, Cambridge University Press, Cambridge **2009**.
[4] I. Moreno, J. A. Davis, M. M. Sánchez-López, K. Badham, D. M. Cottrell, *Opt. Lett.* **2015**, *40*, 5451.
[5] P. Li, Y. Zhang, S. Liu, L. Han, H. Cheng, F. Yu, J. Zhao, *Opt. Lett.* **2016**, *41*, 4811.
[6] P. Li, D. Wu, Y. Zhang, S. Liu, Y. Li, S. Qi, J. Zhao, *Photonics Res.* **2018**, *6*, 756.
[7] S. Fu, S. Zhang, C. Gao, *Sci. Rep.* **2016**, *6*, 30765.
[8] S. Liu, S. Qi, P. Li, B. Wei, P. Chen, W. Hu, Y. Zhang, X. Gan, P. Zhang, Y. Lu, *Laser Photonics Rev.* **2022**, *16*, 2100291.
[9] K. Huang, H. Liu, F. J. Garcia-Vidal, M. Hong, B. Luk'yanchuk, J. Teng, C.-W. Qiu, *Nat. Commun.* **2015**, *6*, 7059.
[10] J. Li, Y. Zhang, J. Li, X. Yan, L. Liang, Z. Zhang, J. Huang, J. Li, Y. Yang, J. Yao, *Nanoscale* **2019**, *11*, 5746.
[11] N. Yu, P. Genevet, M. A. Kats, F. Aieta, J.-P. Tetienne, F. Capasso, Z. Gaburro, *Science* **2011**, *334*, 333.
[12] L. Huang, X. Chen, H. Muhlenbernd, G. Li, B. Bai, Q. Tan, G. Jin, T. Zentgraf, S. Zhang, *Nano Lett.* **2012**, *12*, 5750.
[13] S. Kruk, B. Hopkins, I. I. Kravchenko, A. Miroshnichenko, D. N. Neshev, Y. S. Kivshar, *APL Photonics* **2016**, *1*, 030801.
[14] C. Meng, P. C. Thrane, F. Ding, S. I. Bozhevolnyi, *Nat. Commun.* **2022**, *13*, 2071.
[15] R. C. Devlin, A. Ambrosio, N. A. Rubin, J. B. Mueller, F. Capasso, *Science* **2017**, *358*, 896.
[16] H. Zhou, B. Sain, Y. Wang, C. Schlickriede, R. Zhao, X. Zhang, Q. Wei, X. Li, L. Huang, T. Zentgraf, *ACS Nano* **2020**, *14*, 5553.
[17] A. Arbabi, Y. Horie, M. Bagheri, A. Faraon, *Nat. Nanotechnol.* **2015**, *10*, 937.
[18] Z. L. Deng, M. Jin, X. Ye, S. Wang, T. Shi, J. Deng, N. Mao, Y. Cao, B. O. Guan, A. Alù, *Adv. Funct. Mater.* **2020**, *30*, 1910610.
[19] Y. Bao, Q. Weng, B. Li, *Laser Photonics Rev.* **2022**, *16*, 2100280.
[20] W. T. Chen, M. Khorasaninejad, A. Y. Zhu, J. Oh, R. C. Devlin, A. Zaidi, F. Capasso, *Light: Sci. Appl.* **2017**, *6*, e16259.
[21] X. Zhang, L. Huang, R. Zhao, Q. Wei, X. Li, G. Geng, J. Li, X. Li, Y. Wang, S. Zhang, *Laser Photonics Rev.* **2022**, *16*, 2100451.
[22] W. T. Chen, A. Y. Zhu, V. Sanjeev, M. Khorasaninejad, Z. Shi, E. Lee, F. Capasso, *Nat. Nanotechnol.* **2018**, *13*, 220.
[23] S. Wang, P. C. Wu, V.-C. Su, Y.-C. Lai, M.-K. Chen, H. Y. Kuo, B. H. Chen, Y. H. Chen, T.-T. Huang, J.-H. Wang, *Nat. Nanotechnol.* **2018**, *13*, 227.
[24] L. Huang, X. Chen, H. Mühlenbernd, H. Zhang, S. Chen, B. Bai, Q. Tan, G. Jin, K.-W. Cheah, C.-W. Qiu, *Nat. Commun.* **2013**, *4*, 2808.
[25] G. Zheng, H. Mühlenbernd, M. Kenney, G. Li, T. Zentgraf, S. Zhang, *Nat. Nanotechnol.* **2015**, *10*, 308.
[26] R. Zhao, L. Huang, Y. Wang, *PhotoniX* **2020**, *1*, 20.
[27] G. Li, S. Chen, N. Pholchai, B. Reineke, P. W. H. Wong, E. Y. B. Pun, K. W. Cheah, T. Zentgraf, S. Zhang, *Nat. Mater.* **2015**, *14*, 607.
[28] S. S. Kruk, L. Wang, B. Sain, Z. Dong, J. Yang, T. Zentgraf, Y. Kivshar, *Nat. Photonics* **2022**, *16*, 561.
[29] N. A. Rubin, G. D'Aversa, P. Chevalier, Z. Shi, W. T. Chen, F. Capasso, *Science* **2019**, *365*, eaax1839.
[30] N. A. Rubin, P. Chevalier, M. Juhl, M. Tamagnone, R. Chipman, F. Capasso, *Opt. Express* **2022**, *30*, 9389.
[31] S. Chen, Z. Xie, H. Ye, X. Wang, Z. Guo, Y. He, Y. Li, X. Yuan, D. Fan, *Light: Sci. Appl.* **2021**, *10*, 222.
[32] F. Yue, D. Wen, J. Xin, B. D. Gerardot, J. Li, X. Chen, *ACS Photonics* **2016**, *3*, 1558.
[33] Y. Bao, J. Ni, C. W. Qiu, *Adv. Mater.* **2020**, *32*, 1905659.
[34] Y. Zhang, X. Yang, J. Gao, *Sci. Rep.* **2019**, *9*, 19656.
[35] M. Liu, P. Huo, W. Zhu, C. Zhang, S. Zhang, M. Song, S. Zhang, Q. Zhou, L. Chen, H. J. Lezec, *Nat. Commun.* **2021**, *12*, 2230.
[36] F. Ding, B. Chang, Q. Wei, L. Huang, X. Guan, S. I. Bozhevolnyi, *Laser Photonics Rev.* **2020**, *14*, 2000116.
[37] H. Gao, Y. Wang, X. Fan, B. Jiao, T. Li, C. Shang, C. Zeng, L. Deng, W. Xiong, J. Xia, *Sci. Adv.* **2020**, *6*, eaba8595.
[38] Q. Song, A. Baroni, R. Sawant, P. Ni, V. Brandli, S. Chenot, S. Vézian, B. Damilano, P. de Mierry, S. Khadir, *Nat. Commun.* **2020**, *11*, 2651.
[39] I. Kim, J. Jang, G. Kim, J. Lee, T. Badloe, J. Mun, J. Rho, *Nat. Commun.* **2021**, *12*, 3614.
[40] R. Zhao, B. Sain, Q. Wei, C. Tang, X. Li, T. Weiss, L. Huang, Y. Wang, T. Zentgraf, *Light: Sci. Appl.* **2018**, *7*, 95.
[41] E. Arbabi, S. M. Kamali, A. Arbabi, A. Faraon, *ACS Photonics* **2019**, *6*, 2712.
[42] D. Wen, J. J. Cadusch, J. Meng, K. B. Crozier, *Nano Lett.* **2021**, *21*, 1735.
[43] N. A. Rubin, A. Zaidi, A. H. Dorrah, Z. Shi, F. Capasso, *Sci. Adv.* **2021**, *7*, eabg7488.
[44] Q. Song, X. Liu, C.-W. Qiu, P. Genevet, *Appl. Phys. Rev.* **2022**, *9*, 011311.
[45] A. H. Dorrah, N. A. Rubin, A. Zaidi, M. Tamagnone, F. Capasso, *Nat. Photonics* **2021**, *15*, 287.
[46] Q. Wei, L. Huang, X. Li, J. Liu, Y. Wang, *Adv. Opt. Mater.* **2017**, *5*, 1700434.
[47] G.-Y. Lee, G. Yoon, S.-Y. Lee, H. Yun, J. Cho, K. Lee, H. Kim, J. Rho, B. Lee, *Nanoscale* **2018**, *10*, 4237.
[48] G. Makey, Ö. Yavuz, D. K. Kesim, A. Turnalı, P. Elahi, S. Ilday, O. Tokel, F. Ö. Ilday, *Nat. Photonics* **2019**, *13*, 251.
[49] S.-Y. Lu, R. A. Chipman, *J. Opt. Soc. Am. A* **1996**, *13*, 1106.
[50] Z. Shi, N. A. Rubin, J.-S. Park, F. Capasso, *Phys. Rev. Lett.* **2022**, *129*, 167403.
[51] T. Chang, J. Jung, S. H. Nam, H. Kim, J. U. Kim, N. Kim, S. Jeon, M. Heo, J. Shin, *Adv. Mater.* **2022**, *34*, 2204085.